Investigation of precast RC beam-column assemblies under column-loss scenario

Hussein M. Elsanadedy [*,1], Tarek H. Almusallam, Yousef A. Al-Salloum, Husain Abbas

Chair of Research and Studies in Strengthening and Rehabilitation of Structures, Dept. of Civil Engineering, College of Engineering, King Saud University, P.O. Box 800, Riyadh 11421, Saudi Arabia

HIGHLIGHTS

- Progressive collapse of precast RC beam-column joints was numerically investigated.
- Three specimens tested under middle column-loss scenario were used for validation.
- Tests included two precast specimens and one monolithic specimen.
- Revised precast RC beam-column joint details were numerically investigated.
- New joint efficiency parameters are proposed for progressive collapse assessment.

ARTICLE INFO

ABSTRACT

The progressive collapse of reinforced concrete (RC) buildings, being one of the most critical failure scenarios, is a great concern for the structural engineering community. As precast concrete buildings are deficient in structural continuity, these are more vulnerable to progressive collapse than cast-in-situ RC buildings. The goal of this study is to develop a nonlinear finite element (FE) model using LS-DYNA software to predict the performance of precast non-prestressed RC beam-column assemblies, each comprising three columns and two beams, under column-removal scenario. The model takes into account the nonlinear behavior of concrete and steel, strain rate effect on material properties and contact between surfaces at the joints. The FE models were calibrated against three half-scale specimens tested under middle column-removal scenario. Tests included two precast specimens and one monolithic specimen with continuous top and bottom beam reinforcement. The validated FE modeling was further extended to study the progressive collapse potential of seven revised precast connections. As a result of the FE study, new joint efficiency parameters were introduced in this research.

© 2017 Elsevier Ltd. All rights reserved.

1. Introduction

In the last few decades, precast concrete structural systems have become more common as they are cost-efficient and offer competitive alternatives to cast-in-situ concrete elements. As compared to monolithic reinforced concrete (RC) construction, the advantages of precast concrete systems include: (i) reduced formwork and scaffolding, (ii) reduced skilled labor, (iii) higher speed of construction, (iv) reduced construction waste, (v) flexibility in the shape of the members, and (vi) improved quality and good surface finishing.

Buildings are extremely susceptible to progressive collapse in the event of the removal of columns as a result of exposure to blast generated waves or other extreme load cases such as vehicle crash on a column, seismic excitation or fire. Progressive collapse of structures is generally defined as the progressive spread of a local structural failure to adjoining members and eventually leading to complete or partial collapse of the building. Progressive collapse of a structure usually causes great loss of life and property. As the precast RC buildings greatly lack in the structural continuity and redundancy in the load paths, these are more vulnerable to progressive collapse as compared to the conventional cast-in-situ RC structures. The performance of the precast concrete system depends on the behavior of connections, especially between beams and columns. The configuration of connections affects the constructability, stability, strength, flexibility, energy dissipation capacity, displacement ductility and residual forces in the

---

* Corresponding author.
  E-mail address: elsanadedy@yahoo.com (H.M. Elsanadedy).
[1] On leave from Helwan University, Cairo, Egypt.

structure. Examples of typical precast RC beam-column connections used in Saudi Arabia are given in Fig. 1.

The behavior of different types of precast RC beam-column joints has been investigated by numerous researchers [1–5]. In these studies, different designs for precast joints were studied which included: (i) connections using dowel rebars, (ii) dowel rebars with steel cleat angles, (iii) steel cleat angles with stiffeners, (iv) tie rods and steel plates, (v) use of cast-in-situ concrete in beam-column connection, (vi) bolted connections, (vii) composite connection with welding, etc. In these studies, the behavior of precast connections was evaluated in terms of load-displacement characteristics. The performance was then compared with their monolithic counterparts.

Hawileh et al. [6] studied numerically the behavior of precast hybrid beam-column connections subjected to cyclic loads using nonlinear finite element (FE) modeling. The precast post-tensioned RC beam-column connection was modeled using 3D solid elements and the contact between the beam-to-column faces was modeled using surface-to-surface contact elements. The model response was validated with their previous test results. Kaya and Arslan [7] performed experiments on post-tensioned precast RC beam-column joints at varying stress levels under cyclic loads. The connections were numerically simulated using 3D non-linear FE analysis to determine their load-displacement characteristics. It was concluded that modeling of these types of connections using 3D FE method could give better insight and to some extent eliminate the requirements of time consuming experiments.

One of the approaches to evaluate progressive collapse is to study the effects of sudden removal of vertical load-carrying members (such as a column) on the rest of the structure, and to check if any other alternate load paths exist thereby arresting the damage initiation from propagating from one element to another. Research on progressive collapse of structures was conducted by Allen and Schriever [8], Almusallam et al. [9], Elsanadedy et al. [10], Baldridge and Humay [11], Choi and Chang [12], Al-Salloum et al. [13], Dat et al. [14], Bao et al. [15], and others but these studies are related to the framed buildings. Sasani et al. [16] evaluated the progressive collapse potential of an actual 10-story RC structure due to sudden removal of an exterior column as a result of blast load scenario. The results showed that the structure resisted progressive collapse due to the redistribution of loads as result of Vierendeel action in the transverse frame whose exterior column was removed. Yu and Tan [17] investigated the effect of seismic detailing on structural behavior under a column-loss scenario. Two half-scale monolithic RC beam-column sub-assemblages were designed and detailed according to the seismic and non-seismic specifications. In a study by Li and Sasani [18], the influence of seismic detailing on the progressive collapse potential of RC frame buildings was assessed. The role of strength and ductility capacity of structures when exposed to seismic excitations and to the column-removal scenario were discussed and highlighted. The effect of variation in span on structural response under column-loss scenario was also investigated. Wang et al. [19] studied experimentally the progressive collapse resistance and failure mechanisms and modes of an RC frame with specially shaped columns subjected to middle column removal. It was concluded that the redistribution of internal force was mainly realized via the beam resisting mechanism and the compressive arch action in beams played an important role in improving the collapse-resistance capacity.

Kang and Tan [20] carried out an experimental study to investigate the behavior of precast RC beam-column test specimens under column-loss scenario. The beams and columns were joined together by cast-in-situ concrete topping above the two adjoining beams and the joint. The top longitudinal rebars passed through the joint continuously. The middle joint detailing involved 90° bend and lap-splice of bottom rebars. The specimens were tested to failure under quasi-static loads. It was concluded that the continuity of top reinforcement along with the cast-in-situ concrete topping led to the development of compressive arch action (CAA) and catenary action. However, the CAA and catenary action capacities were overestimated due to the rigid boundary conditions adopted in experiments. In another study, Kang et al. [21] studied the progressive collapse behavior of precast RC beam-column sub-assemblages produced using engineered cementitious composites (ECC) in cast-in-situ structural toppings and joints under column-loss scenarios. Results of the experiments indicated that the development of CAA and catenary action was sequential with increasing vertical joint displacement. Unlike conventional cast-in-situ RC, structural ECC topping showed multi-cracking behavior with distributed cracks.

Nimse et al. [22] investigated experimentally the behavior of three different types of one-third scale precast RC beam-column connections under column-loss scenario. The test specimens with monolithic joints were also tested for the sake of comparison. Precast RC beam-column connections were designed by varying connection details. The behavior of test specimens was assessed in terms of the load-displacement characteristics. Authors reported higher peak load and ductility in precast connections as compared to the monolithic connections.

Maya et al. [23] conducted a two-stage experimental program to evaluate the feasibility of developing continuity connections between precast RC elements based on the use of steel reinforcement with short splice lengths and ultra high performance fiber reinforced concrete (UHPFRC). In the first stage, flexural tests were
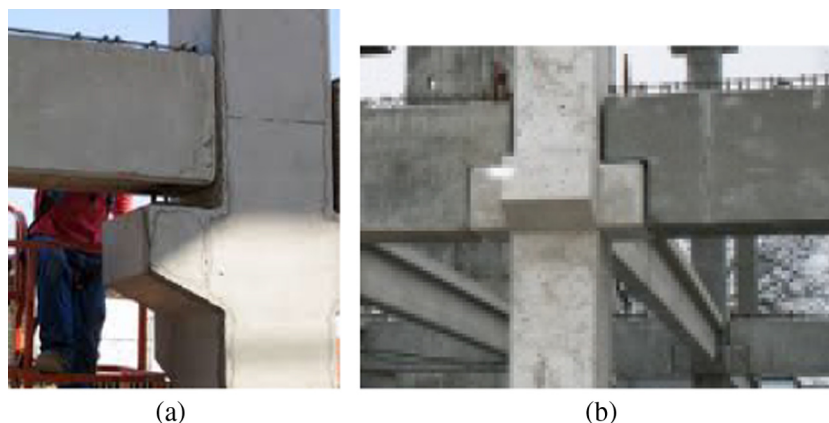

(a) (b)

Fig. 1. Typical precast RC beam-column connections in buildings of Saudi Arabia: (a) Precast connection type-A; (b) Precast connection type-B.

carried out on precast RC beam specimens; whereas in the second stage, precast RC beam-column connection specimens were tested. Magliulo et al. [24] investigated numerically using the FE method the shear behavior of precast RC beam-column dowel connections, typical of European precast industrial buildings. The developed FE models were validated by results of shear monotonic tests on a dowel precast RC beam-beam connection. The validated FE modeling was further extended to study the effect of different variables on the performance of connection and the reliability of some available formulae for the prediction of the dowel connection strength.

It is worth mentioning that although the above studies have provided valuable experimental and numerical data on the progressive collapse behavior of RC beam-column connections, but these studies are primarily limited to either monolithic connections [14–19] or certain types of wet precast connections [20–22]. The aim of this study is, however, to investigate the precast RC beam-column assemblies with different types of dry connections under a column-loss scenario. Although many columns and/or other structural elements may be affected by the blast loads but the design codes [25–29] suggest the consideration of notional single column-removal scenario at design stage for keeping the structural design affordable. This load case represents a possible scenario of explosion involving a suitcase-bomb whose effect may be localized and limited to causing damage to a single column leading to its removal.

An experimental program was conducted by the authors at King Saud University to study the response of two types of half-scale precast non-prestressed assemblies, each comprising three columns and two beams, under middle column-loss scenario. These assemblies represented the most prevalent types of existing precast RC beam-column joints in Saudi Arabia. One cast-in-situ test specimen having continuity of top and bottom beam rebars was used for the sake of comparison. The test specimens were tested under middle column-loss scenario with the middle column being exposed to high rate dynamic loading at a displacement rate of 100 mm/s in order to simulate the progressive collapse in real structures. Performance of precast test specimens was investigated and compared with the cast-in-situ test specimen.

The objective of this research is to develop a finite element (FE) model using LS-DYNA software [30] to predict the behavior of precast non-prestressed RC beam-column connections under column-removal scenario. The simulated FE model takes into account the nonlinear material behavior, strain rate effect on material properties and contact between surfaces at the joints. The results of the numerical study were validated with the test results. Although the experimental studies are ideal to investigate the performance of structures but these are time consuming and costly. Thus, the properly validated computational models could be an attractive alternative to rather expensive experiments. The validated FE modeling was used for some useful parametric studies in which the effect of different revised precast connection details on the response of test frames under middle column-loss scenario was investigated.

2. Experimental study

In order to achieve the goal of this research, experimental data has to be obtained and then used for FE validation. In this regard, three half-scale specimens, tested under column-removal scenario, have been used. The concrete dimensions and reinforcement details of the test specimens are depicted in Table 1 and Fig. 2. Two specimens (PC-A & PC-B) were precast non-prestressed with beams and columns cast individually and then assembled to simulate the field conditions. The other specimen MC-SMF was

Table 1
Details of specimens used for FE validation.[*]

Specimen ID	Type	Beam details		Column details		Corbel details		Beam-column connection details
		Dimensions (mm) $(b \times h \times L)$	Reinforcement	Dimensions (mm) $(b \times h \times H)$	Reinforcement	Dimensions (mm) $(b \times h \times L)$	Reinforcement	
PC-A	Precast type A	350 × 350 × 2620	• 4φ16 mm top & bottom • φ8 mm stirrups @ 100 mm o.c	350 × 350 × 1750	• 8φ16 mm main steel • φ8 mm ties @ 100 mm o.c	350 × 250 × 200	• 4φ16 mm top & bottom • 4φ10 mm closed stirrups	• Beam resting on 20 mm thick neoprene pad attached to the corbel • 1φ16 mm corbel rebar grouted with the beam on both beam ends
PC-B	Precast type B	350 × 350 × 2620	• 4φ16 mm top & bottom • φ8 mm stirrups @ 100 mm o.c	350 × 350 × 1750	• 8φ16 mm main steel • φ8 mm ties @ 100 mm o.c	350 × 250 × 200	• 4φ16 mm top & bottom • 4φ10 mm closed stirrups	• Beam resting on 20 mm thick steel plate welded to two preinstalled steel angles; one attached to the dapped beam end and the other one affixed to the corbel before concrete casting • 1φ16 mm corbel rebar grouted with the beam on both beam ends
MC-SMF	Monolithic	350 × 350 × 2650	• 4φ16 mm top & bottom • φ8 mm stirrups @ 100 mm o.c	350 × 350 × 1750	• 8φ16 mm main steel • φ8 mm ties @ 100 mm o.c	–	–	Monolithic with continuous top and bottom beam reinforcement

[*] b = width of beam (column or corbel) section; h = depth of beam (column or corbel) section; L = beam (or corbel) net span; H = column height.
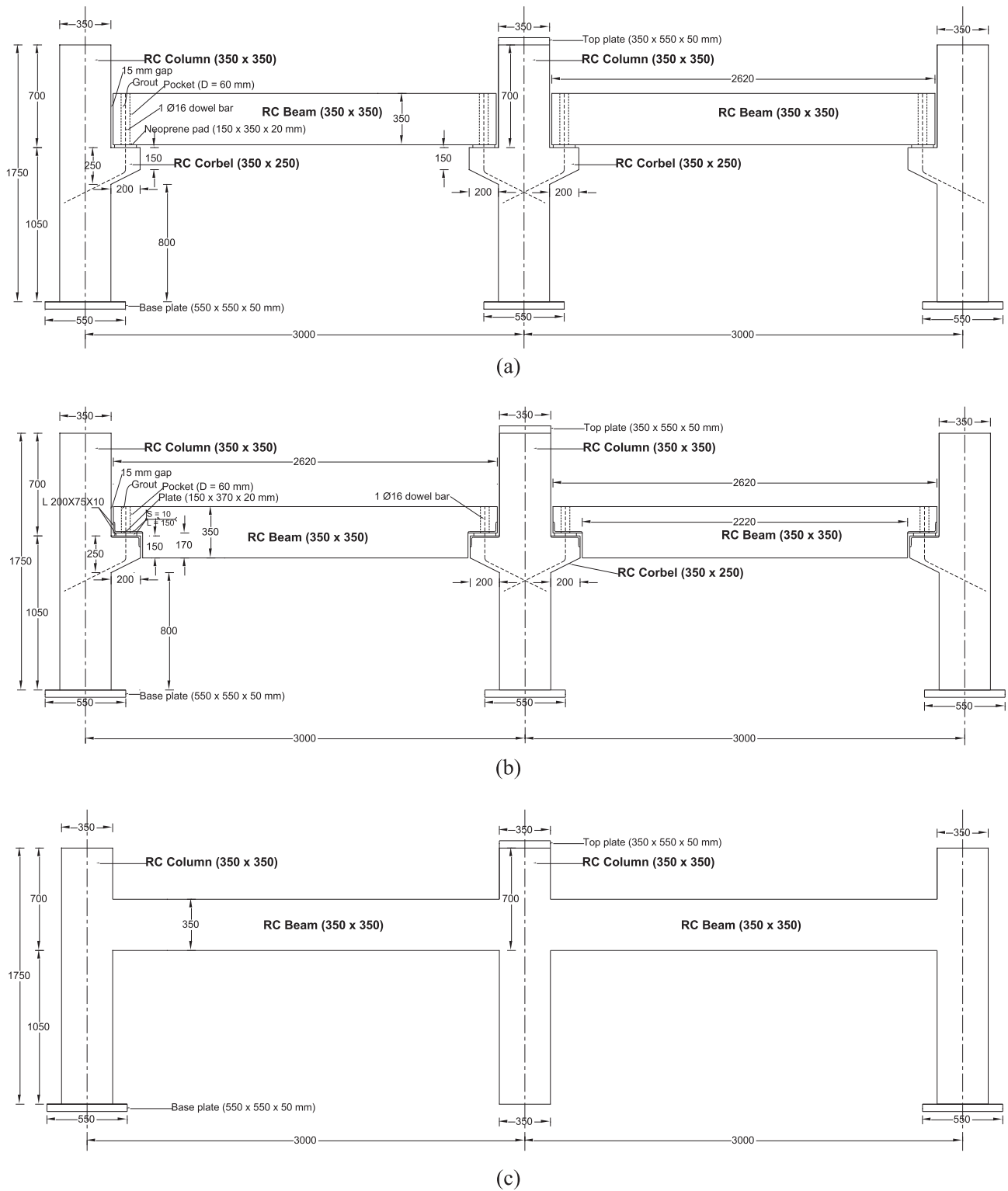
Fig. 2. Concrete dimensions of test specimens (Note: All dimensions are in mm): (a) Specimen PC-A; (b) Specimen PC-B; (c) Specimen MC-SMF.

monolithic with continuous top and bottom beam rebars through the joint region. All specimens consisted of two-bay frames having two beams and three columns. Special test rig was used to support the specimens and displacement controlled loading was applied to the middle column until the failure of specimens. The precast specimens PC-A and PC-B had almost the same dimensions and details;

however, they differed from each other in terms of beam-column connection details. For both columns and beams, section sizes of 350×350 mm were used and the corbels had section dimension of 350×250 mm (Table 1). The total height of the RC column was 1750 mm. The height of the column to the bottom of the beam was 1050 mm and the columns were made to rest on a steel

I-shaped stub of height 500 mm. The steel stubs were connected to steel rails made of I-sections, which were anchored to the strong test floor.

Longitudinal reinforcement of beams comprised of 4φ16 mm rebars on both top and bottom faces and 2 legged φ8 mm rebars used as stirrups at a uniform spacing of 100 mm center-to-center. The longitudinal reinforcement for columns comprised of 8φ16 mm rebars, and φ8 mm ties were provided as transverse reinforcement at a uniform spacing of 100 mm center-to-center, as listed in Table 1. The center-to-center distance between columns

was kept as 3 m. In PC-A specimen, beams rested on 20-mm thick neoprene pad attached to the corbel. The PC-A beam-column connection was composed of a corbel rebar grouted with the beam on both the beam ends. Two pockets of diameter 60 mm were left out at both the beam ends for grouting purposes. For precast specimen PC-B, beams rested on 20-mm thick steel plate welded to two pre-installed steel angles; one attached to the dapped beam end and the other one affixed to the corbel before concrete casting. The angles were spot welded to the longitudinal steel rebars of either beam or corbel. In addition to the welded plate-angles assembly,

Table 2
Material properties used in the FE modeling.

| Concrete & cementitious grout				
Material model	Type 159 (MAT_CSCM_CONCRETE)			
Density (kg/m³)	2320			
Uni-axial compressive strength (MPa)	35 for concrete & 60 for cementitious grout			
Steel rebars, angles & plates	*φ8*	*φ10*	*φ16*	*Angles & plates*
Material model	Type 24 (MAT_PIECEWISE_LINEAR_PLASTICITY)			
Density (kg/m³)	7850			
Young's modulus (GPa)	200			
Poisson's ratio	0.3			
Strain rate parameter, C	250			
Strain rate parameter, p	1.6			
Yield stress (MPa)	525	489	526	240
Tangent modulus (MPa)	127	2127	1065	0
Plastic strain to failure (%)	19.7	11.6	11.7	20
Neoprene pads				
Material model	Type 77 (MAT_HYPERELASTIC_RUBBER)			
Density (kg/m³)	1100			
Poisson's ratio	0.499			
Shear modulus (MPa)	1.38			
Limit stress (MPa)	5.52×10^{-3}			
Constant C_{10}	0.55			
Constant C_{01}	0			
Constant C_{11}	0			
Constant C_{20}	−0.05			
Constant C_{02}	0			
Constant C_{30}	0.95			
Steel stubs at base of columns				
Material model	Type 1 (MAT_ELASTIC)			
Density (kg/m³)	7850			
Young's modulus (GPa)	200			
Poisson's ratio	0.3			
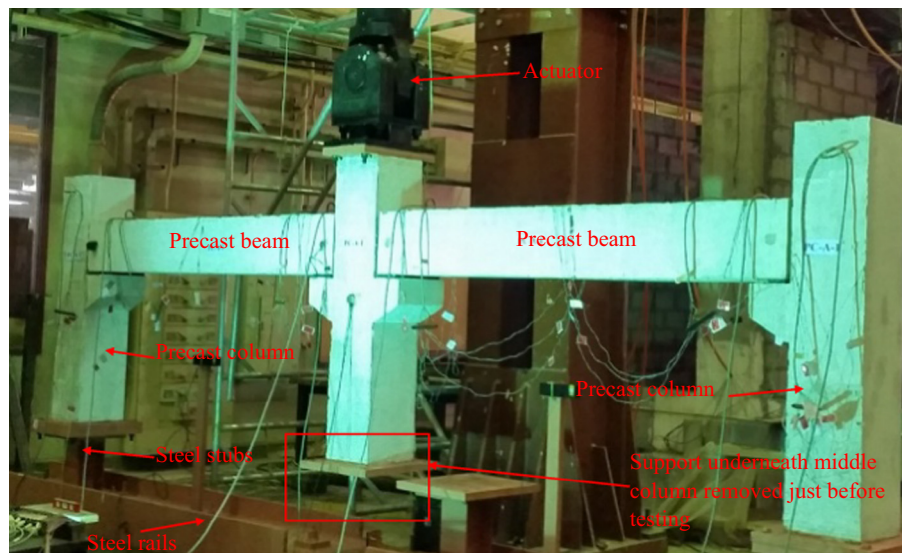
Fig. 3. Test setup for precast specimen PC-A.

1φ16 mm dowel corbel rebar grouted with the beam on both beam ends was used to form the beam-column connection for specimen PC-B.

Ready-mix concrete was used for casting the test specimens. The specified compressive strength, measured as per ASTM C39/C39M [31] at the time of the test, was 35 MPa. For steel rebars, tensile tests were carried out in accordance with ASTM E8/E8M [32] and the average values of yield strength of rebars are reported in Table 2.

The exposure of a building to blast loading may result in the sudden removal of a column, which may lead to the progressive collapse of the structure. This was simulated by releasing the support of the middle column and applying a dynamic load on that column using an actuator in cycles of incremental vertical displacement in each cycle (see Fig. 3). The unloading of the specimen involved taking the column from displaced position to the initial position. The rate of loading was 100 mm/s. This loading rate was the maximum possible for the actuator used in the study. The inertial effects in experiments were of smaller scale than expected in a column-removal scenario. However, the increase in stresses due to the inertial forces is partly compensated by the enhanced material strength and thus the error introduced on account of the reduced inertial effects is expected to be small. Test results for all specimens were analyzed to study the collapse mechanism of the entire test frame as well as its individual members.

3. Finite element modeling

LS-DYNA [30], a general-purpose FE software, was used for the numerical FE modeling of the test specimens. The 3D FE model was created using the general-purpose package FEMB PC Pre-Processor 28.0. Only half of the test specimen was modeled to account for the symmetry.

3.1. Geometry and FE mesh

The FE mesh for half of the specimen PC-A is as shown in Fig. 4 (a). Eight-node reduced integration solid hexahedron elements were employed to represent concrete of columns, beams and corbels. It should be noted that in modeling of RC corbels for specimens PC-A & PC-B, the haunches were ignored and a rectangular geometry was used for simplicity. This is not considered critical in assessing the real behavior of the precast specimens, as the load from the beams would be usually transferred to the columns via shear resistance at corbel-to-column interface. This would rely on the area of the corbel's critical section and on the cross-sectional area of corbel horizontal steel passing through the beam-column interface. Since these areas would be the same in both test specimens and FE model, the results would not be affected. The FE model of steel reinforcement for half of specimen PC-A is displayed in Fig. 4(b). The main and transverse steel rebars
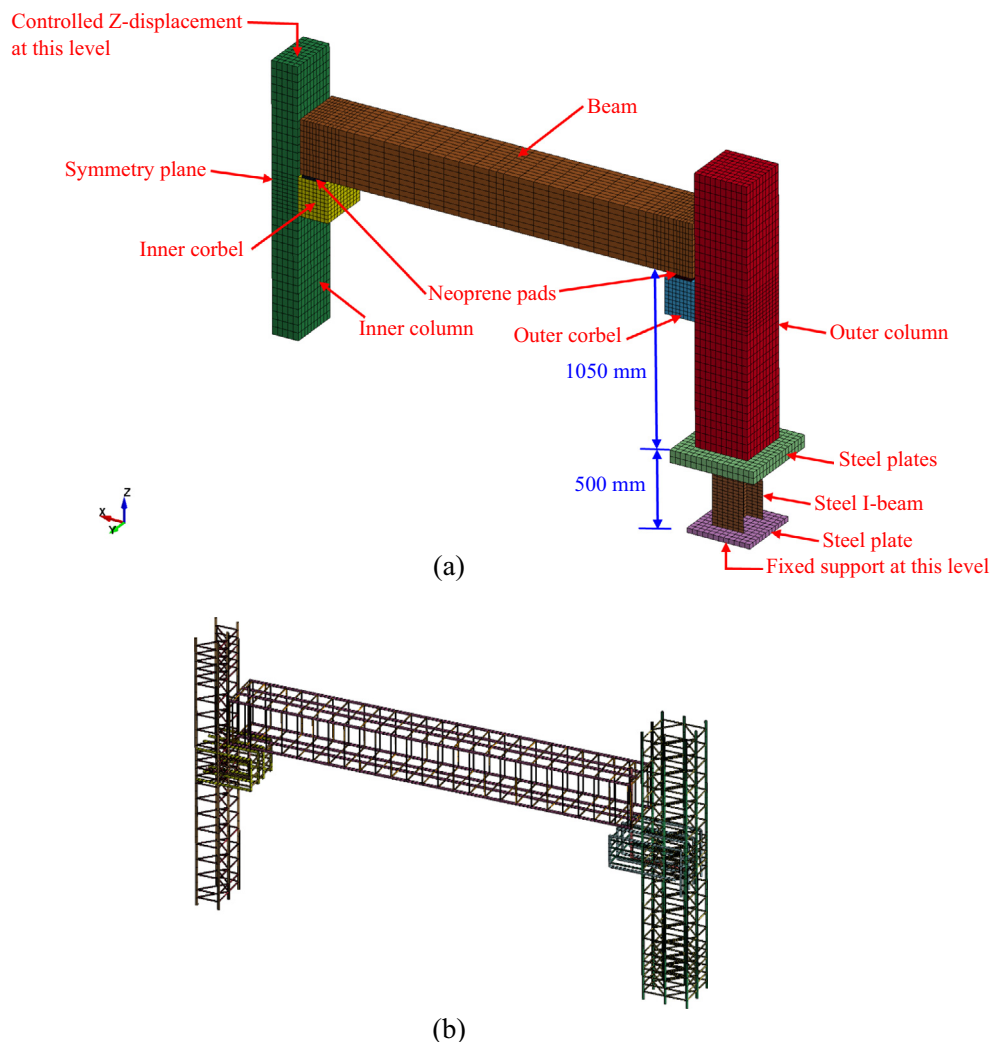

Fig. 4. FE model for precast specimen PC-A: (a) FE mesh for one-half of specimen; (b) FE model of steel reinforcement for one-half of specimen.

of beams, columns and corbels were modeled using 2-node Hughes-Liu beam elements. Eight-node reduced integration solid elements were also used to model both neoprene pads for specimen PC-A and steel plates and angles for specimen PC-B. In order to model the I-shaped steel stubs at column base, solid elements were used to represent steel plates; whereas, the I-beams were modeled using 4-node Belytschko-Tsay shell elements [33], as shown in Fig. 4(a).

Size of elements used in FE mesh varied from 5 to 100 mm. The numerical convergence was investigated and it was found that further refinement of mesh size could have little effect on the numerical results but this may cause computer memory overflow and noticeably increases the computation time. Fig. 4(a) shows the typical mesh of the precast specimen PC-A, which consists of 20,680 solid elements, 4008 beam elements and 360 shell elements to give a total of 25,048 elements.

3.2. Constitutive models

Since the loading was applied dynamically on the test specimens at a rate of 100 mm/s, strain rate effects were included in the material models adopted in this study. Concrete was modeled using MAT_CSCM_CONCRETE (i.e. material model type 159). Smeared crack approach was adopted for simulating the concrete cracking. The model details can be found in reference [34]. The rebars of beams, columns and corbels were modeled using MAT_PIECEWISE_ LINEAR_PLASTICITY (i.e. material model type 24). It was also used to model steel plates and angles at the beam-column connection of specimen PC-B.

The yield stress magnification due to the strain-rate effect was modeled through Cowper-Symonds relation:

$$y = 1 + \left(\frac{\dot{\varepsilon}}{C}\right)^{1/p} \tag{1}$$

where $\dot{\varepsilon}$ is the strain rate. The model parameters C and p were taken as 250 and 1.6, respectively. For the I-shaped steel stubs at base of columns, the behavior was assumed linear elastic and the material model type 1, MAT_ELASTIC was employed for both plates and steel I-beams. In order to model the neoprene pads of specimen PC-A, the material model type 77, MAT_HYPERELASTIC_RUBBER was used. This material model uses a hyperelastic rubber model, as described
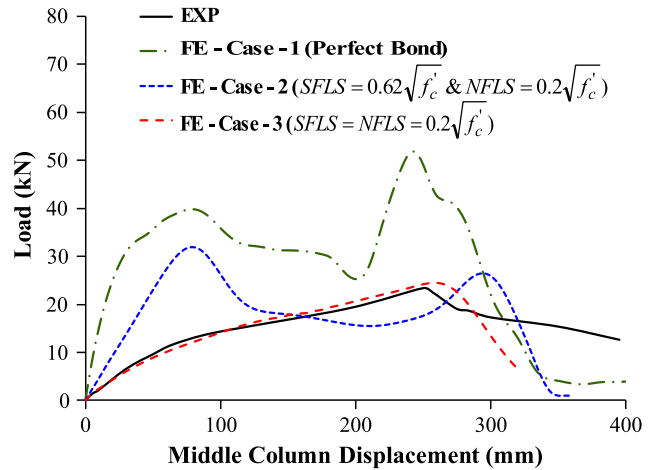
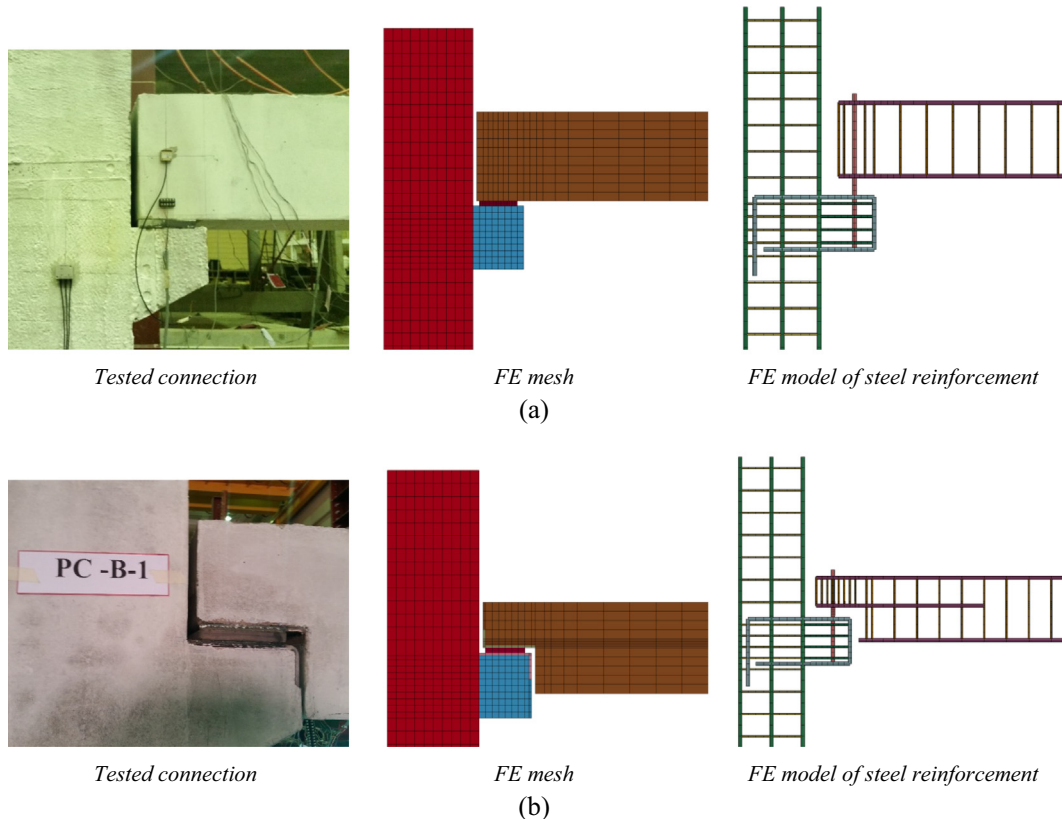**Fig. 6.** Comparison of experimental and FE load-displacement envelopes for specimen PC-B.

Tested connection	*FE mesh*	*FE model of steel reinforcement*
	(a)	

Tested connection	*FE mesh*	*FE model of steel reinforcement*
	(b)	

Fig. 5. Tested precast beam-column connections: Geometry & FE model: (a) Specimen PC-A; (b) Specimen PC-B.
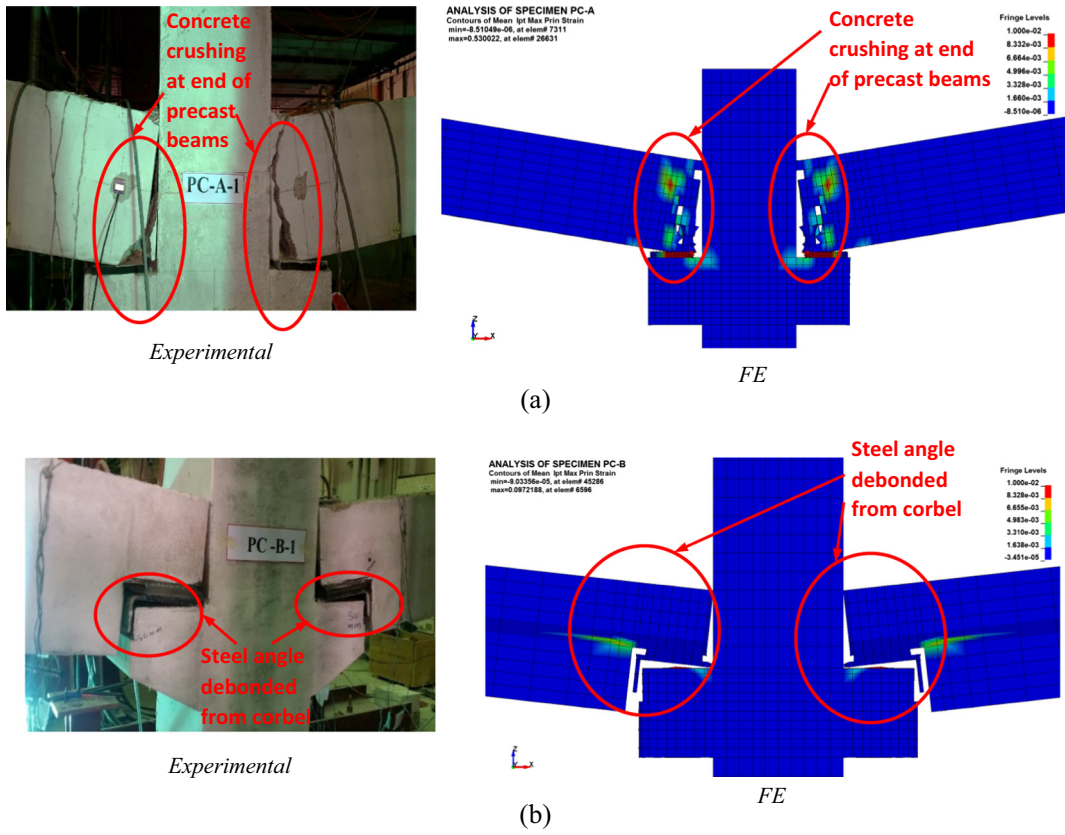
Fig. 7. Comparison of experimental and FE mode of failure of middle joint of: (a) Specimen PC-A; (b) Specimen PC-B.
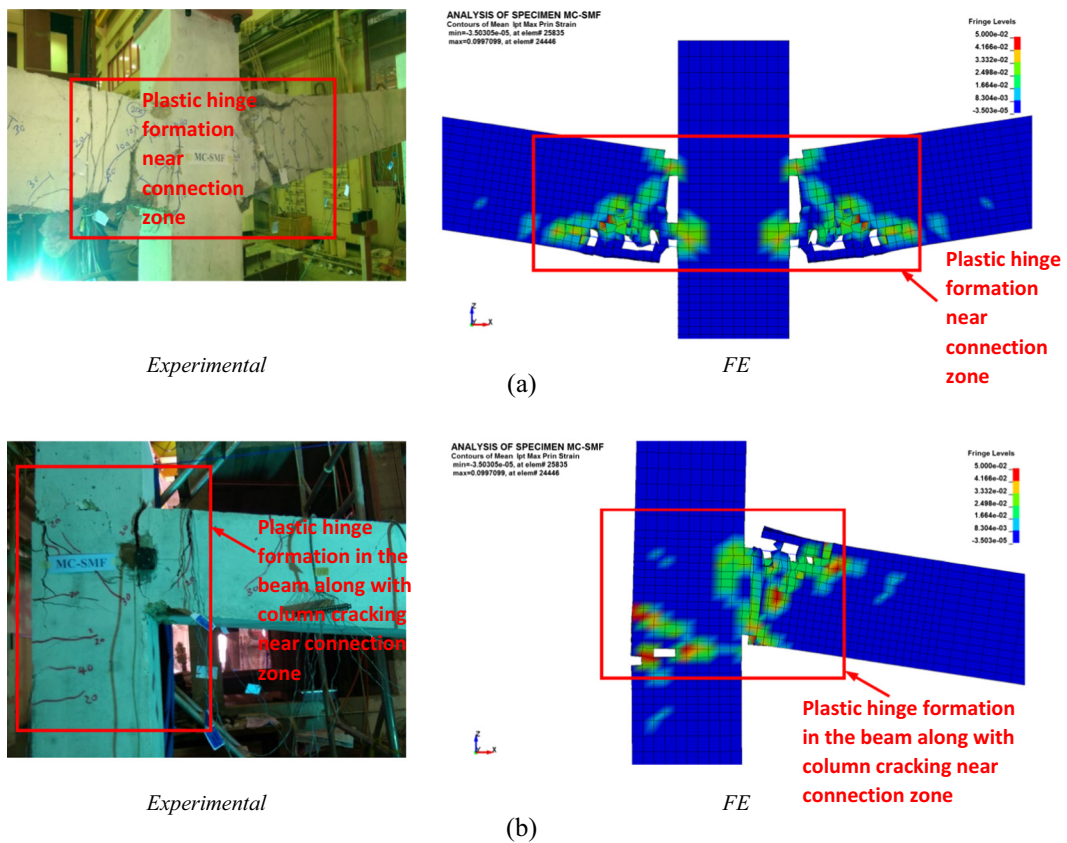

Fig. 8. Comparison of experimental and FE mode of failure for specimen MC-SMF: (a) Failure of middle joint; (b) Failure of end joint.

by Christensen [35]. The material properties used in the FE analysis are given in Table 2.

The strain dependent element erosion was used to simulate the failure of material. This erosion model is a numerical solution for severe element distortions that may result in unrealistic element deformations. Based on the work done by the authors and others [34,36], the maximum principal tensile strain for concrete element erosion was taken as 0.05. For rebars, the plastic tensile strain to failure was used to represent material failure and the erosion was input to start upon material failure.

3.3. Contact modeling

3.3.1. Specimen PC-A

Fig. 5(a) depicts modeled connection of specimen PC-A. A general automatic surface-to-surface contact was assigned between the following pairs: (i) beam and inner column, (ii) beam and outer column, (iii) beam and neoprene pad of inner corbel, (iv) beam and neoprene pad of outer corbel, (v) neoprene pad and inner corbel, and (vi) neoprene pad and outer corbel. For each pair, one surface was taken as master and the other one was taken as slave. Coefficient of friction of 0.6 was assumed between concrete surfaces in contact [37], whereas a coefficient of friction of 0.4 was assumed between neoprene pads and concrete surfaces in contact [38].

3.3.2. Specimen PC-B

Modeled connection of specimen PC-B is displayed in Fig. 5(b). Similar to PC-A, automatic surface-to-surface contacts were assigned between beam and all of inner and outer columns and inner and outer corbels. The CONSTRAINED_GENERALIZED_WELD_FILLET keyword was used to model welding in the connection region between steel plate and the two steel angles attached to the dapped beam end and to the corbel (see Fig. 5(b)). Spot welding between steel angles and rebars of either beam or corbel was ignored and the bond between preinstalled angles and concrete was assumed to rely only on adhesion at the interface, which was modeled using the following failure criterion for tiebreak surface-to-surface contact:

$$\left(\frac{|\sigma_n|}{NFLS}\right)^2 + \left(\frac{|\sigma_s|}{SFLS}\right)^2 \geqslant 1 \tag{2}$$

where σ_n & σ_s are the normal and shear stresses, respectively; and *NFLS* & *SFLS* are the normal and shear failure stresses, respectively. The failure stresses used in current study were determined via calibrating the model parameters against the experimental data of specimen PC-B, as discussed later in Section 4.1.

3.4. Loading and boundary conditions

Taking advantage of the symmetry in the test specimens, only one-half of the test specimen was modeled. The fixed support at the column base was modeled by restricting the displacement and rotation in the global X, Y and Z directions, as shown in Fig. 4(a). The nodes lying on the plane of symmetry were restrained against displacement in the global X direction and the rotation about the global Y and Z directions. The displacement-controlled load was applied at the top surface nodes of the inner column by giving same Z-displacement (see Fig. 4(a)). The rate of increase of vertical displacement of the top of the middle column was 100 mm/s to simulate the experiments.

4. Validation of FE modeling

As mentioned previously, the experimental results of the three specimens were used for the validation of the numerical analysis and the modeling techniques. The results of the numerical study are discussed in the subsequent sub-sections.

4.1. Calibration of contact parameters for specimen PC-B

For specimen PC-B, failure stresses *NFLS* and *SFLS* for the tiebreak contacts used at angles-to-concrete interface were determined by calibrating the FE model results against the experimental load-displacement envelope. Three FE cases were studied. The first case (case-1) is an upper bound in which perfect bond was assumed between angles and concrete surfaces in contact. In the second case (case-2), failure stresses *NFLS* and *SFLS* were assumed same as those used at fresh-to-hardened concrete interface. In this case and according to Elsanadedy et al. [36] and Silfwerbrand [39], these stresses may be estimated from:

$$NFLS = 0.2\sqrt{f'_c} \text{ (MPa)} \tag{3}$$

$$SFLS = 0.62\sqrt{f'_c} \text{ (MPa)} \tag{4}$$

where f'_c = specified cylinder strength of concrete. In the third case (case-3), the shear failure stress was reduced to be the same as normal failure stress, given by Eq. (3).

Three different FE models were then created for specimen PC-B considering the above-mentioned three cases. The predicted load-displacement curve was generated for each case and then
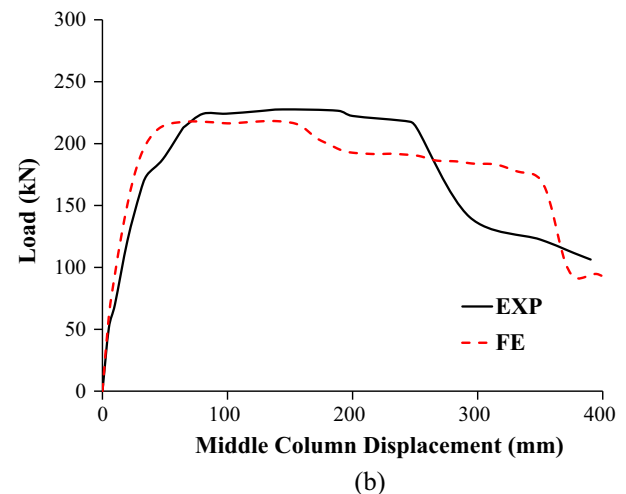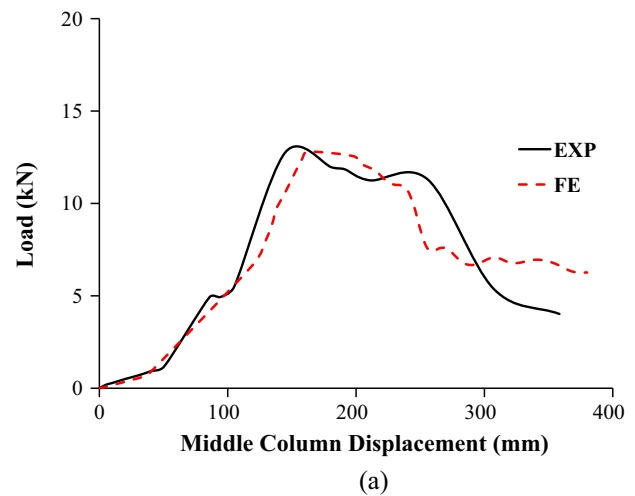

(a)

(b)

Fig. 9. Comparison of experimental and FE load-displacement envelopes for: (a) Specimen PC-A; (b) Specimen MC-SMF.

compared with the experimental one as shown in Fig. 6. It is observed from Fig. 6 that FE model with perfect bond assumption at angles-to-concrete interface (case-1) significantly overestimated both peak load and stiffness with predicted-to-tested peak load ratio of about 2.2. The FE model of case-2 also overestimated both peak load and stiffness with predicted-to-tested peak load ratio of about 1.4. However, the FE model of case-3 gave the best fit to the experimental results in terms of load-displacement characteristics, and thus the right hand side of Eq. (3) was considered successful in estimating normal and shear failure stresses at angles-to-concrete interface of specimen PC-B.

4.2. Mode of failure

Figs. 7(a), (b) and 8 depict the modes of failure for specimens PC-A, PC-B and MC-SMF, respectively, as obtained from the FE analysis post-processing software at the end of the analysis time. The modes of failure in these figures are shown using contours of mid-surface maximum principal strains. It is observed from these figures that the failure modes predicted from the numerical analysis match very well with the experiments. From the analysis it was found that, for specimen PC-A, a proper hinge behavior was observed in the specimen, which was expected. During the analysis, both the beams of specimen PC-A were found to rotate at their ends until the interior ends came in contact with the middle column, and the ultimate mode of failure was due to concrete crushing at the location of interior beam-column connection as seen in Fig. 7(a). No other damage was observed in any members of specimen PC-A including beams and columns.

Fig. 7(b) presents comparison of experimental and FE failure modes of middle beam-column connection of specimen PC-B. A good match was found between the experimental and predicted

Table 3
Comparison of experimental and FE load-displacement characteristics for test specimens.[*]

Specimen ID	Results	P_u (kN)	$\Delta_{u,c}$ (mm)	$\Delta_{u,b}$ (mm)	P_y (kN)	Δ_y (mm)	Δ_u (mm)	E_u (kN.m)
PC-A	EXP	12.8	145	66	NY	NY	265	2.5
	FE	12.8	160	77	NY	NY	243	2.6
	EXP/FE	1.00	0.91	0.86	–	–	1.09	0.97
PC-B	EXP	23.4	250	116	NY	NY	284	5.5
	FE	24.5	260	120	NY	NY	285	5.0
	EXP/FE	0.96	0.96	0.97	–	–	1.00	1.10
MC-SMF	EXP	228	144	65	145	25.6	269	65.9
	FE	218	145	70	153	21	335	67.4
	EXP/FE	1.04	0.99	0.93	0.95	1.25	0.80	0.98

[*] P_u = peak load; $\Delta_{u,c}$ = middle column displacement at peak load; $\Delta_{u,b}$ = beam mid-span deflection at peak load; P_y = load at yielding of bottom beam steel; Δ_y = middle column displacement at yielding of bottom beam steel; Δ_u = middle column displacement at ultimate state; E_u = energy dissipated; EXP = experimental; FE = finite element; NY = No steel yielding.
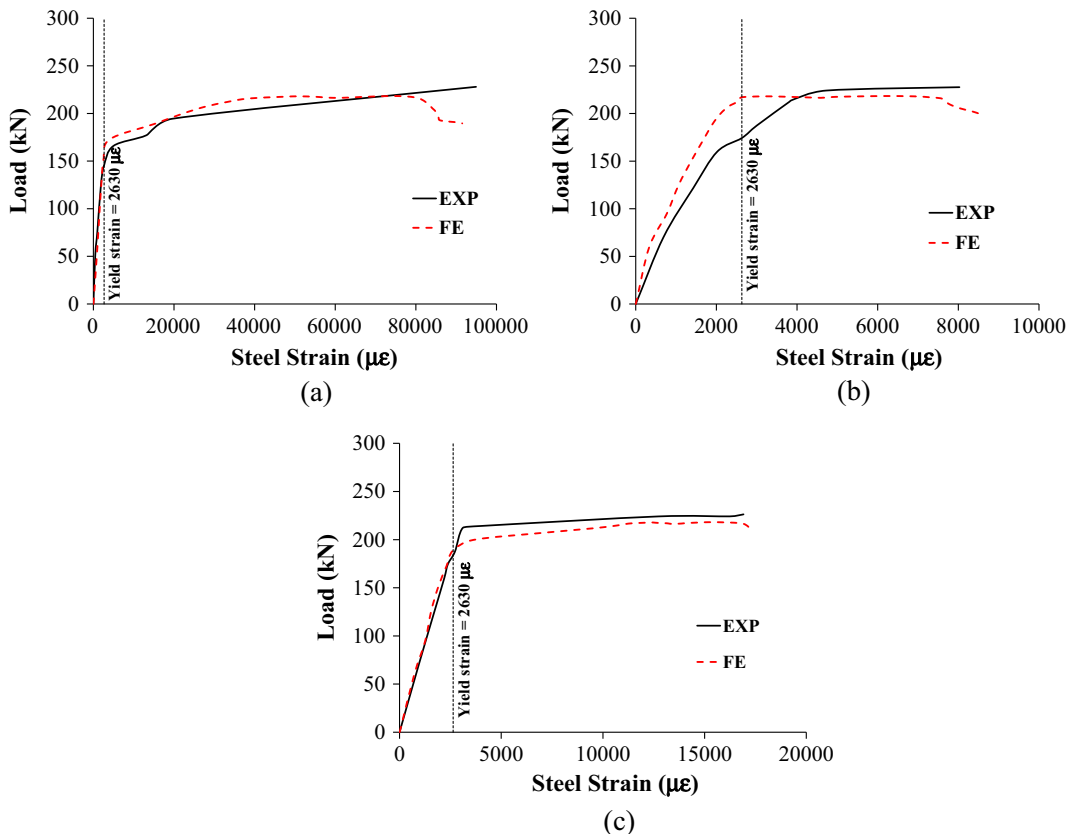

Fig. 10. Comparison of experimental and FE load vs. steel strain curves for specimen MC-SMF: (a) Bottom rebars of beam at face of inner column; (b) Top rebars of beam at face of outer column; (c) Outer rebars of exterior column near connection zone.

failure modes for the PC-B frame. A proper hinge behavior was noticed and the left and right beams were found to rotate at their ends until failure occurred due to debonding of steel angles of the corbels near the interior column. Some minor cracks were also formed in the corbels of the middle column.

Fig. 8 depicts the experimental failure mode for the monolithic MC-SMF frame as compared to the predicted one. As seen from Fig. 8, good agreement was noted between the experimental and FE modes of failure. A plastic hinge was formed in the beam area near the middle connection zone as indicated by wide flexural cracks accompanied with concrete crushing in the compression zone (Fig. 8(a)). At the exterior joint, plastic hinge formation occurred in the beam along with column cracking near connection zone as displayed in Fig. 8(b).

4.3. Load-displacement characteristics

Figs. 6 and 9 depict a comparison between the load versus middle column displacement envelopes obtained from the numerical and the experimental studies for the three test specimens. The figures show good agreement between the numerical and experimental load-displacement curves especially for the peak load for the two precast specimens as well as the monolithic specimen.

Table 3 enlists the comparison details in terms of load-displacement characteristics. As seen from Table 3, deviation of 0−4% is observed in the numerical prediction of peak loads. However, compared with the experimental results, deviations of 1%−9%, 3%−14% and 0%−20% were observed for middle column displacement at peak load, beam mid-span deflection at peak load, and middle column displacement at ultimate state, respectively. As

seen from Table 3, the energy dissipated (area under load-displacement curve up to a displacement equal to the total depth of the beam (350 mm in this study)) was predicted efficiently by the FE modeling with deviation ranging from 2% to 10%. As depicted from Figs. 6 and 9, the stiffness of the test specimens at all levels of loading was also predicted well by the numerical models in comparison with the experiments. Figs. 6 and 9 clearly show that the numerical models were effective in simulating the softening behavior, which establishes the precision of the material models.

The FE analysis also revealed that precast connection type B is relatively better than connection type A in terms of its resistance to progressive collapse. However, compared with the monolithic specimen MC-SMF, the two connections were found to have a very high potential of progressive collapse due to negligible ductility and lack of continuity in beam-column joints and hence absence of redundancies in the load paths. According to both experimental and FE results, it was concluded that even though the monolithic specimen with continuous top and bottom beam reinforcement had significantly higher ultimate load and energy dissipated compared to two precast specimens, the development of catenary action was inhibited due to: discontinuity of beams beyond the exterior columns and the insufficient restraint provided by outer columns.

4.4. Strain gage analysis

Fig. 10 shows the comparison between numerical and experimental values of maximum tensile strain in the main rebars for monolithic specimen MC-SMF. Table 4 shows rebar strains

Table 4
Comparison of experimental and FE peak strains for test specimens.[*]

| Specimen ID	Results	Longitudinal rebars of beam		Outer rebars of exterior column	Top rebars of inner corbel	Dowel rebars of inner corbel
		Bottom rebars at face of inner column (or corbel)	Top rebars at face of outer column (or corbel)			
PC-A	EXP	74	60	50	247	NA
	FE	58	41	62	330	36,616
	EXP/FE	1.28	1.45	0.80	0.75	–
PC-B	EXP	622	475	153	556	NA
	FE	732	456	166	759	151,078
	EXP/FE	0.85	1.04	0.92	0.73	–
MC-SMF	EXP	95,189	14,957	16,912	–	–
	FE	102,065	13,183	17,236	–	–
	EXP/FE	0.93	1.13	0.98	–	–

[*] EXP = experimental; FE = finite element; NA = not available data.

Table 5
Details of FE matrix used in the parametric study.

Specimen ID	Type	Beam-column connection details
PC-A-WA	Revised precast type A	Same as PC-A with the replacement of neoprene pads with 20 mm thick steel plates welded to two preinstalled steel angles; one attached to the beam end and the other one attached to the corbel (see Fig. 11)
PC-A-PBA	Revised precast type A	Same as PC-A-WA specimen but with perfect bond assumption at angles-to-concrete interface
PC-A-PBA-G	Revised precast type A	Same as PC-A-PBA specimen but with filling the gap between beams and columns with non-shrink modified cementitious grout
PC-A-PBA-G-TA	Revised precast type A	Same as PC-A-PBA-G specimen with the addition of top steel angle welded to both steel angle perfectly bonded with beam top end and steel plate perfectly bonded with column concrete (see Fig. 12)
PC-B-PBA	Revised precast type B	Same as PC-B specimen but with perfect bond assumption at angles-to-concrete interface
PC-B-PBA-G	Revised precast type B	Same as PC-B-PBA specimen but with filling the gap between beams and columns with non-shrink modified cementitious grout
PC-B-PBA-G-TA	Revised precast type B	Same as PC-B-PBA-G specimen with the addition of top steel angle welded to both steel angle perfectly bonded with beam top end and steel plate perfectly bonded with column concrete (see Fig. 13)

obtained numerically and experimentally for three test specimens. Good agreement between the numerical and experimental values was obtained. From Table 4, it is clear that both measured and predicted strains for specimen PC-B were larger than those for precast specimen PC-A, which supported the conclusion mentioned earlier about the superiority of specimen PC-B to specimen PC-A in terms of its resistance to progressive collapse.

The strains for steel rebars of both precast specimens were significantly low due to the discontinuity of bottom beam reinforcement at the connection zone, and hence the disability of precast specimens to dissipate the energy. Thus both precast specimens PC-A & PC-B are very much vulnerable to progressive collapse. However, for monolithic specimen MC-SMF and as presented in Fig. 10 and Table 4, all tension steel rebars (at the ends of beams
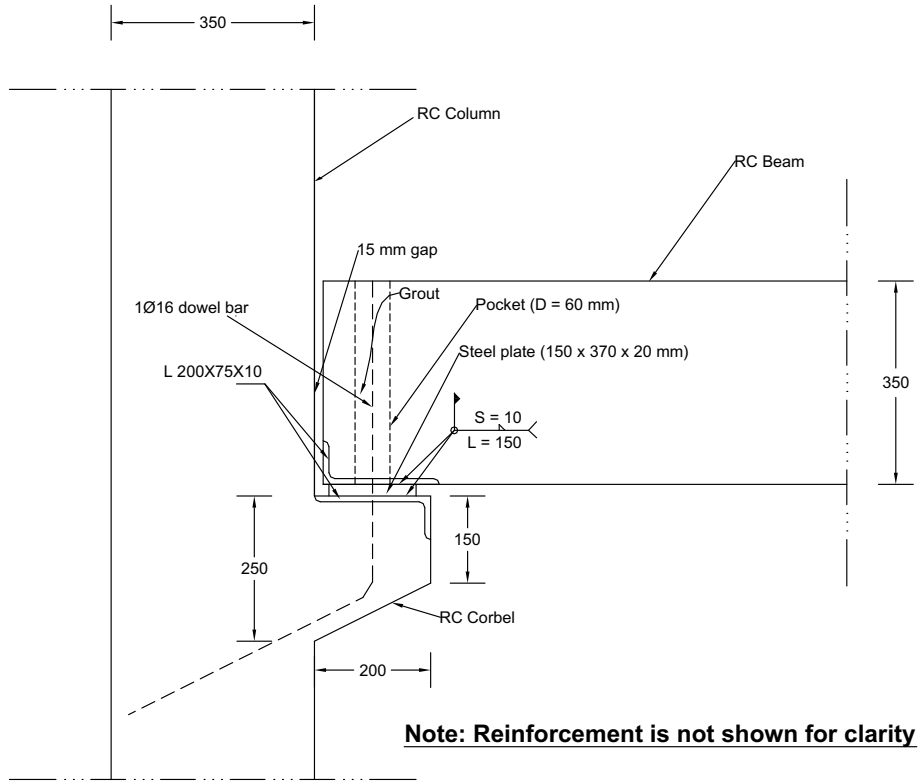
(a)
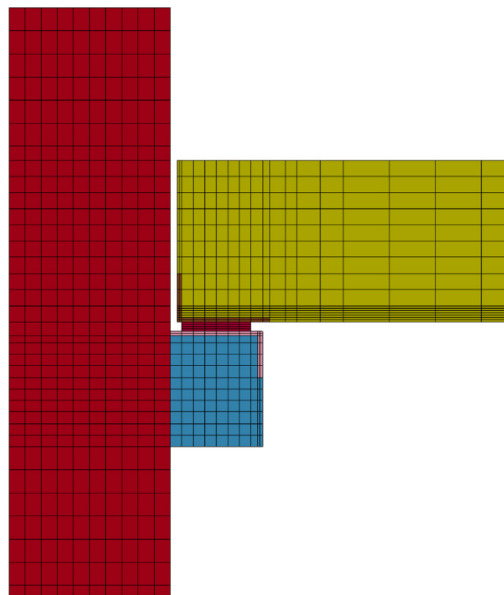
(b)

Fig. 11. Beam-column connection for specimen PC-A-WA: (a) Details (Note: All dimensions are in mm); (b) FE model.

and at outer columns near connection zone) had yielded and large tensile strains were noted, thereby indicating plastic hinge formation at the ends of beams, as previously outlined.

5. Effect of revised details of precast connections

The validated FE modeling was further extended to study the effect of different revised details of precast connections on the behavior of tested frames under middle column-removal scenario. Seven specimens with revised connection details, as displayed in Table 5, were analyzed. The specimens included 4 revised connec-

tions of original precast specimen PC-A and 3 revised connections for the precast specimen PC-B. As both experimental and FE studies revealed that precast connection type B is relatively better than connection type A in terms of its resistance to progressive collapse, a new specimen (PC-A-WA) was numerically studied. Details of beam-column connection for specimen PC-A-WA are presented in Fig. 11. For specimen PC-A-WA, the original beam-column connection of specimen PC-A was revised through the replacement of neoprene pads with connection similar to that of PC-B specimen (Fig. 11). As the failure of precast specimen PC-B was due to debonding at steel angle-to-corbel interface, special attention has to be paid to the anchorage of angles inside corbel and beam
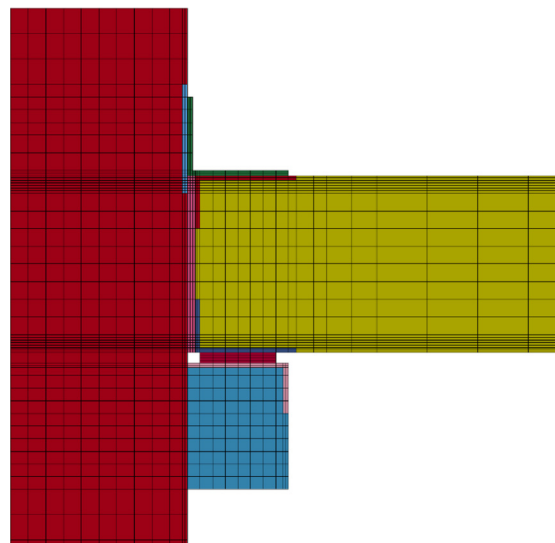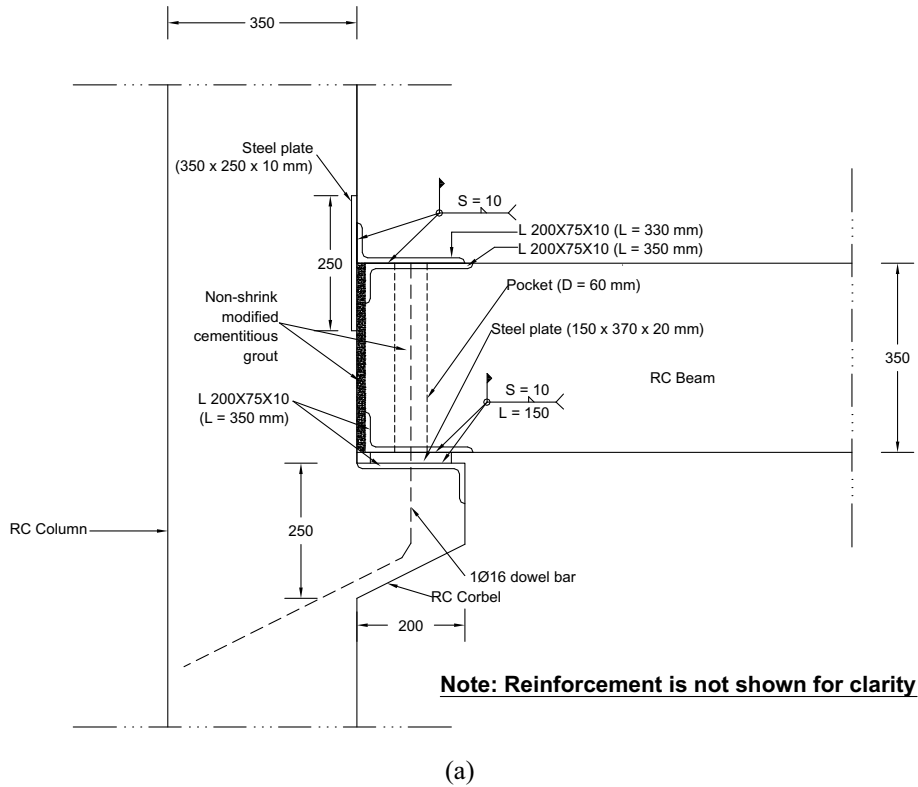

(a)

(b)

Fig. 12. Beam-column connection for specimen PC-A-PBA-G-TA: (a) Details (Note: All dimensions are in mm); (b) FE model.

concrete. Proper anchorage could be achieved in reality through any mechanical means such as using headed high strength rods (or metal studs), welded to the angles and embedded into the concrete before casting. In order to numerically investigate the effect of provision of proper anchorage at steel angles-to-concrete interface, the FE models of specimens PC-A-WA and PC-B were repeated with perfect bond assumption at angles-to-concrete interface as seen in specimens PC-A-PBA and PC-B-PBA, respectively, in Table 5. In order to minimize the rotation at beam ends, two more specimens (PC-A-PBA-G and PC-B-PBA-G) were numerically investigated as seen in Table 5. These two specimens, respectively, were the same as PC-A-PBA and PC-B-PBA specimens but with filling the gap between beams and columns using non-shrink modified cementitious grout.
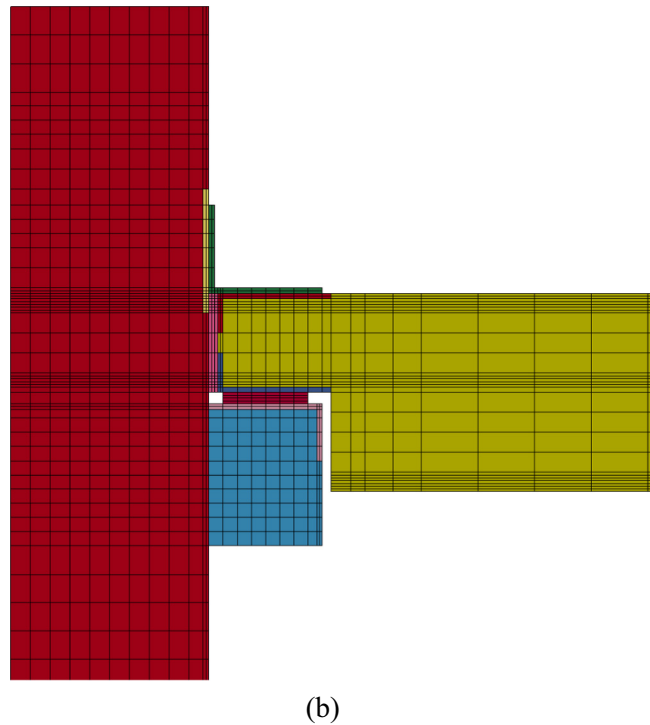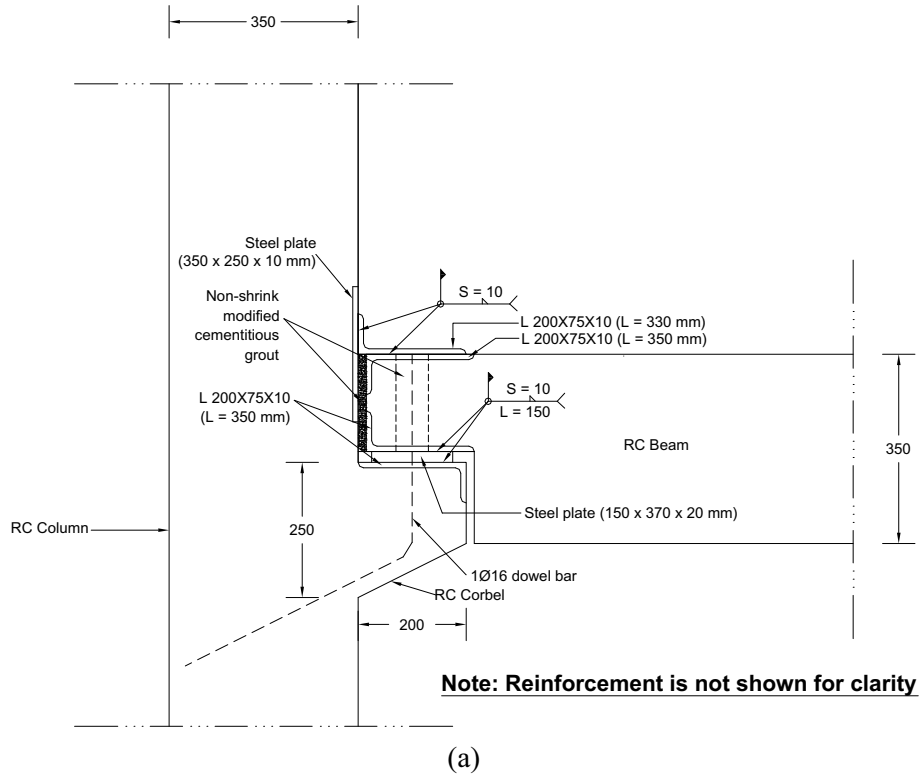

(a)

(b)

Fig. 13. Beam-column connection for specimen PC-B-PBA-G-TA: (a) Details (Note: All dimensions are in mm); (b) FE model.

In this case, 8-node reduced integration solid hexahedron elements were used to model grout volume similar to the concrete volume but with higher compressive strength as displayed in Table 2. Automatic surface-to-surface contacts were assigned between the grout fill and beam-to-column interface with friction coefficient of 0.6 between surfaces in contact. In order to provide continuity of the beam top at column face, two new specimens (PC-A-PBA-G-TA and PC-B-PBA-G-TA) were further studied, as seen in Table 5. They were same as PC-A-PBA-G and PC-B-PBA-G specimens, respectively, with the addition of top steel angle (Figs. 12 (a) and 13(a)). Details and FE models of beam-column connections for specimens PC-A-PBA-G-TA and PC-B-PBA-G-TA are shown in Figs. 12 and 13, respectively. In these two connections, perfect bond was assumed between: (i) steel angles and beam concrete, (ii) steel angle and corbel, and (iii) steel plate and column concrete.

Summary of FE modes of failure for the seven investigated specimens is listed in Table 6. FE mode of failure for representative samples of revised connection specimens are also depicted in Fig. 14. In Table 6 and Fig. 14, failure modes are presented for the inner beam-column connections. Failure of specimen PC-A-WA was almost similar to specimen PC-B, as seen in Fig. 14(a). However, at the middle joint, failure started with debonding at angle-corbel interface (similar to PC-B specimen), then ended up with crushing of concrete at beam end similar to specimen PC-A. Assuming perfect bond at angles-to-concrete interface affected the failure modes of PC-A-PBA and PC-B-PBA specimens. Debonding was inhibited; however, concrete at angles-to-concrete interface got damaged at large displacement levels and failure of the middle joint ended up with concrete crushing at beam end, combined with damage of column concrete cover at beam-column interface. However, for exterior joints, failure ended up with concrete damage at beam end, as detailed in Table 6. As seen in Fig. 14(b) and Table 6, failure of PC-A-PBA-G and PC-B-PBA-G specimens was similar to their un-grouted counterparts PC-A-PBA and PC-B-PBA, but with crushing of infill grout at beam-column interface.

As seen in Table 6, failure of the middle joint of specimen PC-A-PBA-G-TA was different from that of specimen PC-B-PBA-G-TA. In the former, failure was the same as specimen PC-A-PBA-G with the addition of partial damage of column concrete cover at beam-column interface. However, in the middle joint of specimen PC-B-PBA-G-TA, no damage occurred at the beam-column interface and the elements remained intact until the end of the analysis time, but concrete cracking and crushing was noticed in the beam

at section near corbel interface as seen in Fig. 14(c). Failure of exterior joints of PC-A-PBA-G-TA and PC-B-PBA-G-TA specimens was almost identical to their counterparts PC-A-PBA-G and PC-B-PBA-G with the addition of damage of column cover concrete near steel plate-column interface (Table 6).

The FE analysis results of the seven studied specimens are listed in Table 7. Results of the three test specimens used in the FE validation are also given in Table 7 for the sake of comparison. Comparisons between load versus middle column displacement envelopes obtained from the FE modeling are displayed in Fig. 15 (a) and (b) for revised PC-A and PC-B connections, respectively. The load-displacement envelopes for specimens PC-A, PC-B and MC-SMF are also plotted in Fig. 15.

It is generally noted that revising the precast beam-column connection details enhanced the load-displacement characteristics under middle column-removal scenario. It is also noted that peak loads of revised PC-A specimens are considerably higher than those for their revised PC-B counterparts. This is attributed to the reduced beam section for PC-B specimens at corbel interface. Revising the connection detailing of PC-A specimen to make it similar to that of PC-B specimen enhanced both peak load and energy dissipated by 145% and 141%, respectively, as observed from Table 7 and Fig. 15(a) for specimen PC-A-WA. Assuming perfect bond at angles-to-concrete interface increased both peak load and energy dissipated by 244% and 142%, respectively, for specimen PC-A-PBA compared with specimen PC-A-WA. However, perfect bond assumption at angles-to-concrete interface for specimen PC-B-PBA enhanced its peak load and energy dissipated by about 111% and 115%, respectively, compared with specimen PC-B.

Filling up the gap between beams and columns with non-shrink modified cementitious grout enhanced the peak load for specimens PC-A-PBA-G and PC-B-PBA-G by about 24% and 44%, respectively, compared with the corresponding specimens PC-A-PBA and PC-B-PBA. Nevertheless, it had no effect on the energy dissipated in specimen PC-A-PBA-G and it was almost same as that for specimen PC-A-PBA (Table 7). For specimen PC-B-PBA-G, filling up the gap with grout enhanced the energy dissipated by about 53% compared with specimen PC-B-PBA. The provision of continuity at top of beam-to-column interface of specimen PC-A-PBA-G-TA had minimal effect on both peak load and energy dissipated as seen in Table 7 and Fig. 15(a). Compared with specimen PC-A-PBA-G, increases of only 6% and 27% were obtained for peak load and energy dissipated, respectively. However, the enhancement was more noticeable for specimen PC-B-PBA-G-TA, in which the peak

Table 6
Summary of FE mode of failure for specimens used in the parametric study.

| Specimen ID	Damage description at middle joint	Damage description at exterior joint
PC-A-WA	• Concrete crushing at beam end • Debonding at angle-corbel interface	• Debonding at angle-corbel interface • Partial damage of corbel concrete
PC-A-PBA	• Concrete damage at angle-corbel interface • Concrete damage at angle-beam interface • Concrete crushing at beam end • Damage of column concrete cover just above corbel-column junction	• Concrete damage at angle-corbel interface • Concrete damage at angle-beam interface • Concrete crushing at beam end
PC-A-PBA-G	• Concrete damage at angle-corbel interface • Concrete damage at angle-beam interface • Crushing of infill grout • Concrete crushing at beam end • Damage of column cover concrete at beam-column interface	• Concrete damage at angle-corbel interface • Concrete damage at angle-beam interface • Crushing of infill grout • Concrete crushing at beam end
PC-A-PBA-G-TA	• Concrete damage at angle-corbel interface • Partial damage of corbel concrete • Concrete crushing at beam end • Crushing of infill grout • Damage of column concrete cover at beam-column interface	• Concrete damage at angle-corbel interface • Concrete crushing at beam end • Crushing of infill grout • Damage of column cover concrete near plate-column interface
PC-B-PBA	Same as specimen PC-A-PBA	Same as specimen PC-A-PBA
PC-B-PBA-G	Same as specimen PC-A-PBA-G	Same as specimen PC-A-PBA-G
PC-B-PBA-G-TA	Concrete cracking & crushing at beam end at section near corbel interface	Same as specimen PC-A-PBA-G-TA
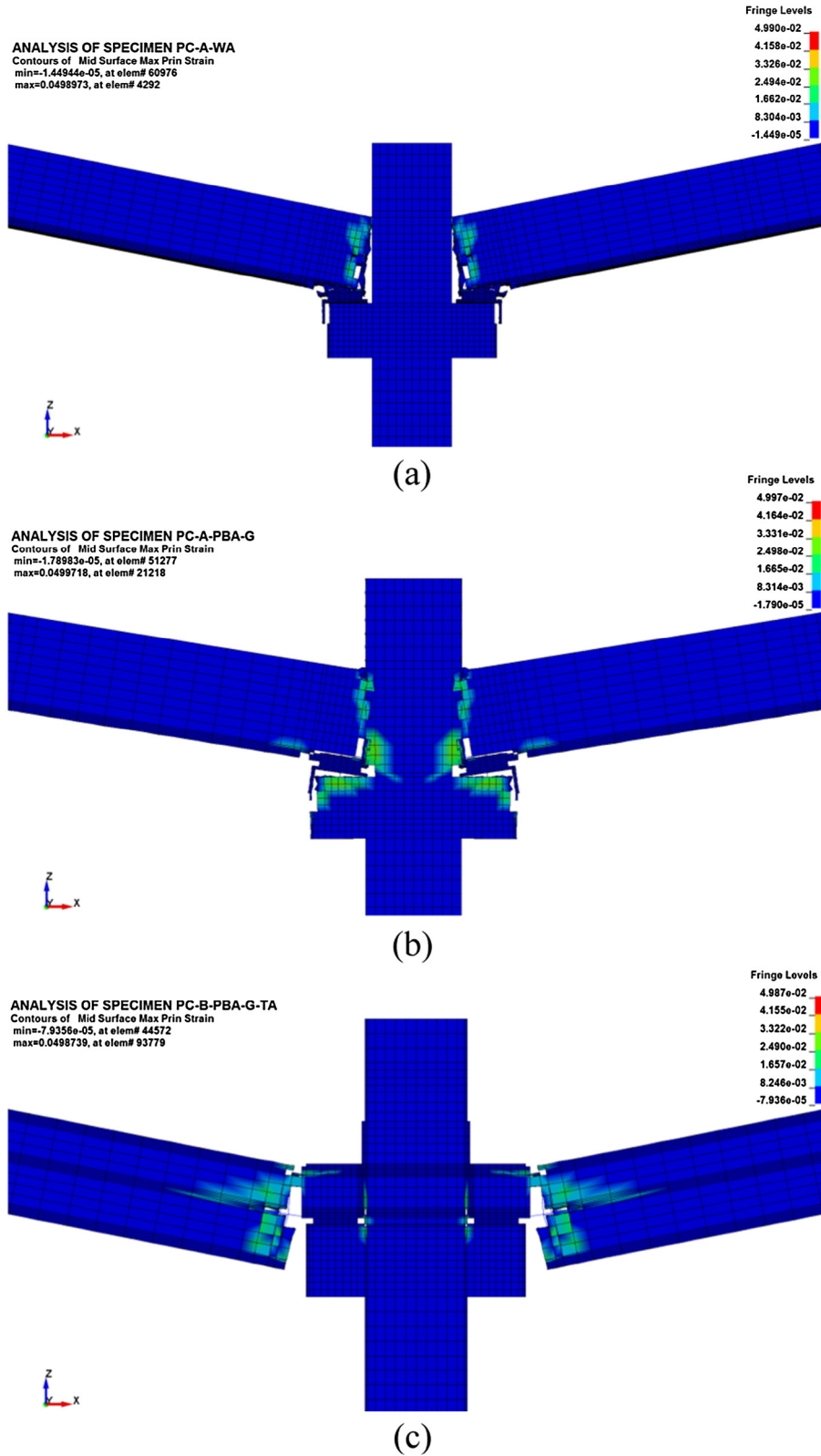
Fig. 14. FE mode of failure of middle joint for representative samples of revised connection specimens: (a) Specimen PC-A-WA; (b) Specimen PC-A-PBA-G; (c) Specimen PC-B-PBA-G-TA.

load and dissipated energy increased by 19% and 55% compared to specimen PC-A-PBA-G, as depicted from Fig. 15(b) and Table 7.

Comparisons between rebar strains at different locations versus middle column displacement curves, obtained from the FE modeling, are presented in Figs. 16 and 17 for revised PC-A and PC-B connections, respectively. Plots for PC-A and PC-B specimens are also included in Figs. 16 and 17, respectively. Peak rebar strains at different locations are summarized in Table 7 for all specimens. Contrary to the monolithic specimen MC-SMF, strains in top rebars of beams at the face of outer corbels were below the yield strain for

Table 7
Summary of FE results for all specimens.[*]

Specimen ID	Peak load (kN)	Middle column displacement at peak load (mm)	Middle column displacement at ultimate state (mm)	Energy dissipated (kN.m)	Peak steel strain (με)				
					Beam bottom rebars at face of inner corbel	Beam top rebars at face of outer corbel	Outer rebars of exterior column	Top rebars of inner corbel	Dowel rebars of inner corbel
PC-A precast specimens									
PC-A	13	160	243	2.5	58	41	62	330	*36,616*
PC-A-WA	31	210	231	6.0	413	87	411	421	*238,092*
PC-A-PBA	108	170	194	14.5	*2674*	148	692	*3569*	*150,554*
PC-A-PBA-G	134	50	58	14.6	*2778*	44	934	*3809*	*100,711*
PC-A-PBA-G-TA	143	45	63	18.6	*3901*	1423	1486	*5240*	*167,331*
PC-B precast specimens									
PC-B	24	260	285	5.0	732	456	166	759	*151,078*
PC-B-PBA	52	245	270	10.7	2065	1592	1057	1025	*106,988*
PC-B-PBA-G	74	80	143	16.3	*13,830*	1649	1126	*2665*	*145,845*
PC-B-PBA-G-TA	89	35	285	25.3	*126,603*	1512	1530	1276	1473
Monolithic specimen									
MC-SMF	218	145	335	67.4	*102,065*	*13,183*	*17,236*	–	–

[*] Values in italic bold font exceed their respective yield strains.
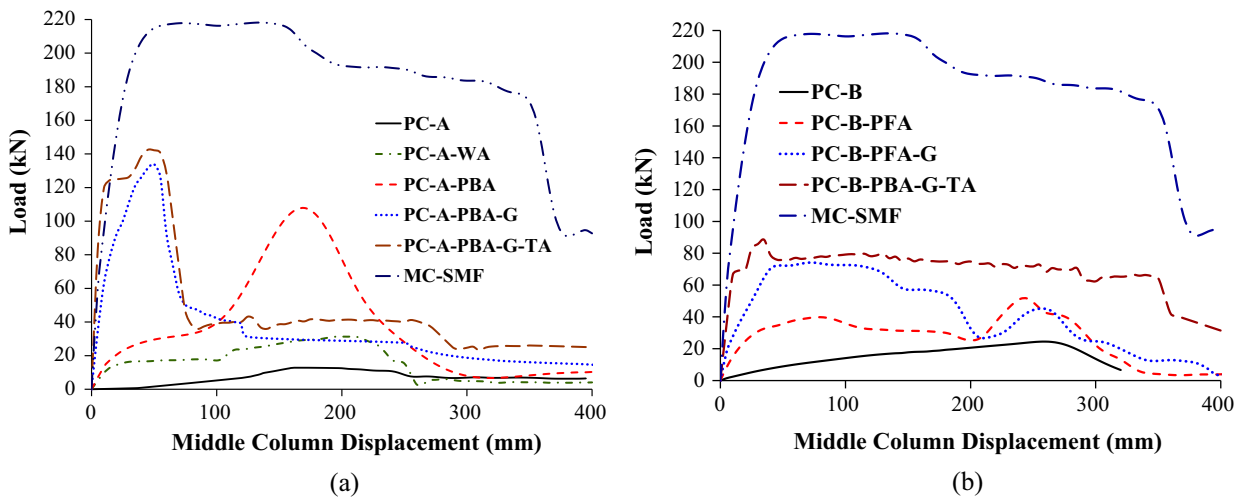

Fig. 15. Load-displacement envelopes for revised precast specimens (based on FE analysis): (a) Revised PC-A specimens; (b) Revised PC-B specimens.
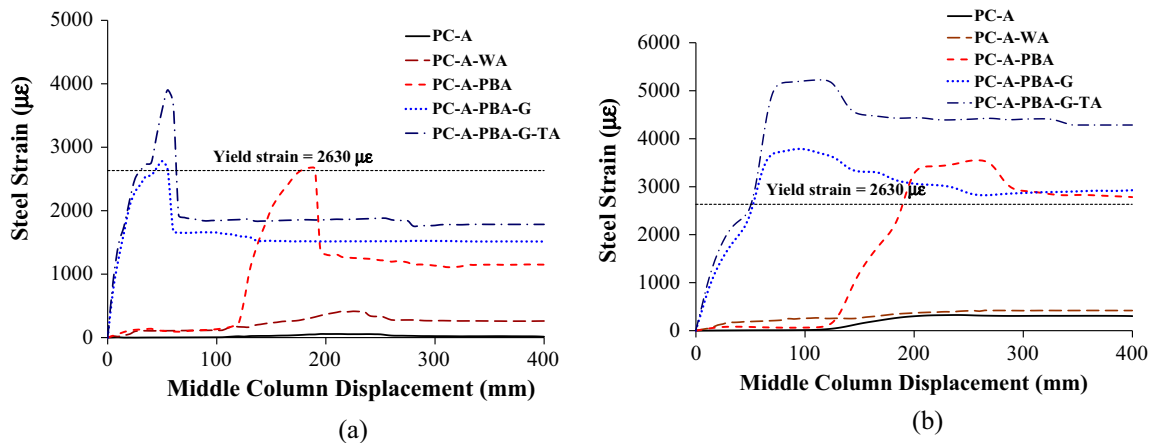

Fig. 16. Steel strain vs. middle column displacement for revised PC-A specimens (based on FE analysis): (a) Bottom rebars of beam at inner corbel face; (b) Top rebars of inner corbel at column face.

all nine precast specimens, as seen in Table 7. In addition, except for the dowel rebars, strains predicted for steel rebars of precast specimens PC-A, PC-A-WA, PC-B and PC-B-PA were lower than the rebar yield strain. Perfect bond assumption at angles-to-

concrete interface for specimen PC-A-PBA enhanced the strain predicted in beam bottom rebars at face of inner corbel, as it reached a value close to its yield strain, as illustrated in Fig. 16(a) and Table 7. Filling up the gap with grout significantly enhanced the strain
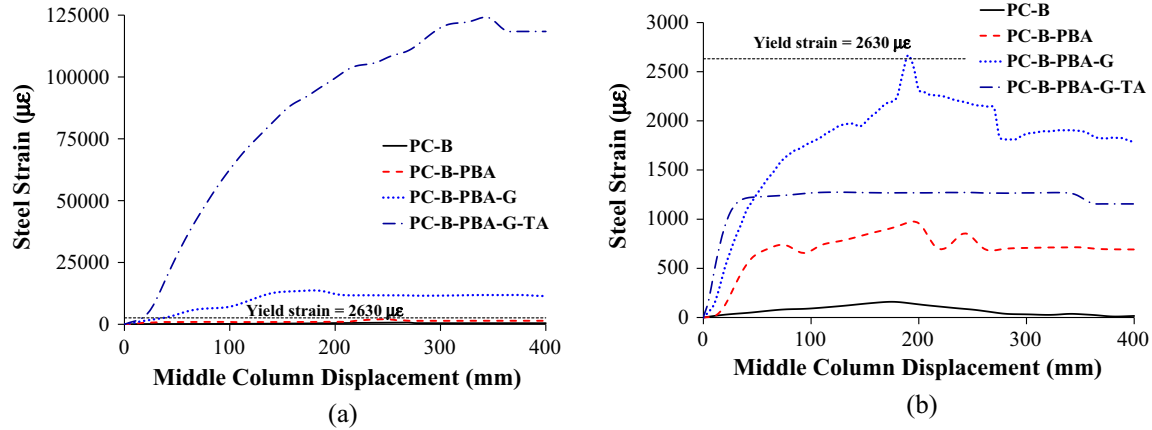
Fig. 17. Steel strain vs. middle column displacement for revised PC-B specimens (based on FE analysis): (a) Bottom rebars of beam at inner corbel face; (b) Top rebars of inner corbel at column face.

predicted for beam bottom rebars at inner corbel face for specimen PC-B-PBA-G, in which the strain reached a value of about 5.3 times the yield strain. The same was not true for specimen PC-A-PBA-G, in which filling up the gap with grout had a negligible effect on strains of beam bottom rebars at inner corbel face, as displayed in Fig. 16(a) and Table 7. Continuity at top of beam-to-column interface of specimen PC-B-PBA-G-TA had remarkable effect on predicted strains of beam bottom rebars at inner corbel face, as shown in Fig. 17(a). Peak strain of about 48 times the yield strain was predicted, as seen in Table 7. The effect of continuity at the top of beam-to-column interface on strain of beam bottom rebars at inner corbel face was not much pronounced for specimen PC-A-PBA-G-TA, as peak strain of about 1.5 times the yield strain was predicted (Fig. 16(a)). As seen from Fig. 16(b), top rebars of inner corbel did not reach their yield strain for specimen PC-A-WA due to the debonding at angle-to-corbel interface. However, due to the perfect bond assumption at angles-to-concrete interface of specimens PC-A-PBA, PC-A-PBA-G and PC-A-PBA-G-TA, yield strains were predicted for the top rebars of inner corbel, as seen in Fig. 16(b) and Table 7.

For specimen PC-B-PBA, even though perfect bond was assumed, top rebars of inner corbel did not reach the yield strain, as seen in Table 7 and Fig. 17(b). This is because the load resisted by this specimen (26 kN transferred by each corbel) was not large enough to cause yielding of corbel rebars. However, for specimen PC-B-PBA-G, the load transferred by each corbel was about 37 kN, which was close enough to cause yielding of top rebars of inner corbel, as depicted from Table 7 and Fig. 17(b). As seen earlier in Fig. 14(c), the dapped ends of the beam remained in full contact with the inner corbels until the end of the analysis time and hence the effective depth of the corbel section at beam-corbel interface got increased thereby reducing the strains of the top corbel rebars. Accordingly, for specimen PC-B-PBA-G-TA, peak strain of top rebars of the inner corbel was only 49% of the yield strain.

In order to help in comparing the performance of revised beam-column connection specimens under middle column-removal scenario, two new parameters were introduced in this study. The first is called the peak load efficiency (η_p) and the second is termed as the energy efficiency (η_E). These new parameters can be expressed as follows:

$$\eta_p = \frac{P_{u,precast}}{P_{u,monolithic}} \times 100\% \tag{5}$$

$$\eta_E = \frac{E_{u,precast}}{E_{u,monolithic}} \times 100\% \tag{6}$$

where $P_{u,precast}$ = peak load of precast specimen; $P_{u,monolithic}$ = peak load of corresponding monolithic specimen with continuous top and bottom beam reinforcement (specimen MC-SMF);
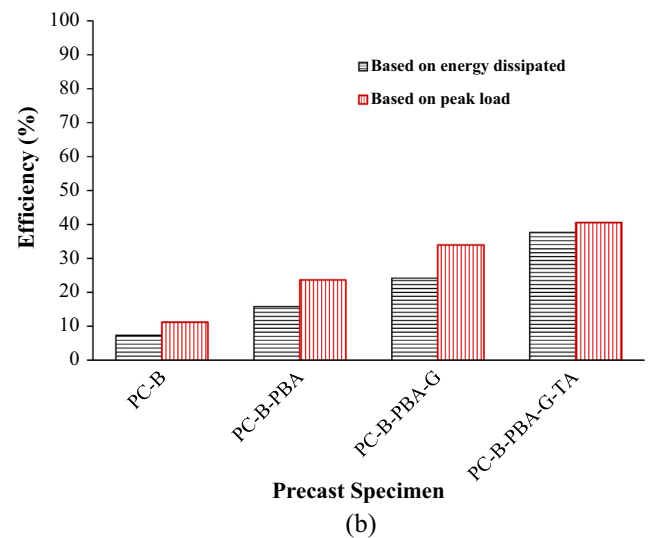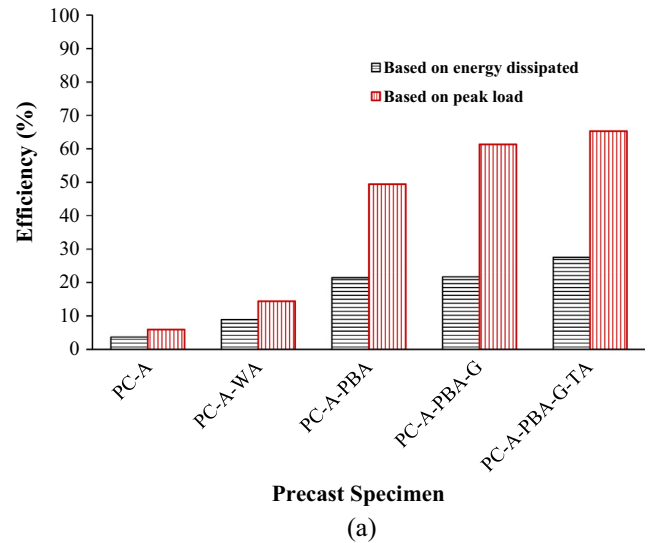

Fig. 18. Effect of connection details on efficiency of precast specimens under column-removal scenario (based on FE analysis): (a) Revised PC-A specimens; (b) Revised PC-B specimens.

$E_{u,precast}$ = energy dissipated in precast specimen = area under load-displacement curve up to a displacement equal to the total depth of the beam (350 mm in this study); and $E_{u,monolithic}$ = energy dissipated for corresponding monolithic specimen with continuous top and bottom beam reinforcement (specimen MC-SMF). The above two parameters were calculated for all precast specimens of this study and are plotted in Fig. 18(a) and (b) for PC-A and PC-B specimens, respectively.

It is shown that due to the reduced beam section for PC-B specimens at corbel interface, their peak load efficiencies were less than those for their PC-A counterparts. As seen in Fig. 18, peak load efficiency for PC-B specimens (PC-B to PC-B-PBA-G-TA) ranged from 11% to 41%; whereas, peak load efficiency for their PC-A counterparts (PC-A-WA to PC-A-PBA-G-TA) ranged from 14% to 65%. However, the energy efficiency for specimens PC-A-WA, PC-A-PBA and PC-A-PBA-G were close to their PC-B counterparts (PC-B, PC-B-PBA and PC-B-PBA-G). Among all precast specimens, the highest energy efficiency (about 38%) was given by specimen PC-B-PBA-G-TA, compared with 28% given by specimen PC-A-PBA-G-TA.

6. Conclusions

The main findings of this study can be summarized as follows:

1. The monolithic specimen with continuous top and bottom beam reinforcement had significantly higher ultimate load and dissipated energy compared to precast specimens. The development of catenary action was inhibited due to the discontinuity of beams beyond the exterior columns and the insufficient restraint provided by outer columns.
2. The existing precast beam-column connections PC-A and PC-B are very vulnerable to progressive collapse once column is removed suddenly in an extreme event. It is therefore highly recommended to improve their connection details using steel plates, angles and headed high strength rods (or metal studs) for connecting the beam ends with the corbel and the column. In addition to these amendments, filling up the gap between beams and columns with non-shrink cementitious mortar is also recommended.
3. The predicted collapse loads of revised PC-A specimens were significantly higher than those for their revised PC-B counterparts. This is attributed to the reduced beam section for PC-B specimens at corbel interface.
4. Two new parameters were introduced in this study. The first is called the peak load efficiency (η_p) and the second is termed as the energy efficiency (η_E). These parameters were utilized for comparing performance of precast beam-column connections under column-removal scenario with monolithic RC connection with continuous top and bottom beam reinforcement. The highest peak load efficiency of 65% was provided by revised precast connection PC-A-PBA-G-TA; however, the highest energy efficiency of 38% was achieved in connection PC-B-PBA-G-TA. Both connections are thus recommended for exterior RC frames of multistory buildings to minimize the progressive collapse potential.
5. The limited energy efficiency provided by revised precast beam-column connections investigated in this study (maximum of 38%) necessitates the search for innovative design of precast moment connections in which continuity is provided using top and bottom beam rebars passing through joint region.

Acknowledgments

References

[1] H.K. Choi, Y.C. Choi, C.S. Choi, Development and testing of precast concrete beam-to-column connections, Eng. Struct. 56 (2013) 1820–1835.
[2] R. Vidjeapriya, K.P. Jaya, Experimental study on two simple mechanical precast beam column connections under reverse cyclic loading, J. Perform. Constr. Facil 27 (2013) 402–414.
[3] R. Vidjeapriya, K.P. Jaya, Behaviour of precast beam-column mechanical connections under cyclic loading, Asian J. Civil Eng. (Build. Hous.) 13 (2014) 233–245.
[4] O. Ertas, S. Ozden, T. Ozturan, Ductile connections in precast concrete moment resisting frames, PCI J 5 (2006) 2–12.
[5] M.K. Joshi, C.V. Murty, M.P. Jaisingh, Cyclic behaviour of precast RC connections, Indian Concr. J. 79 (2005) 43–50.
[6] R.A. Hawileh, A. Rahman, H. Tabatabai, Nonlinear finite element analysis and modeling of a precast hybrid beam-column connection subjected to cyclic loads, Appl. Math. Model. 34 (2010) 2562–2583.
[7] M. Kaya, A.S. Arslan, Analytical modeling of post-tensioned precast beam-to-column connections, Mater. Des. 30 (2009) 3802–3811.
[8] D.E. Allen, W.R. Schriever, Progressive Collapse, Abnormal Load, and Building Codes, Structural Failure: Modes, Causes, Responsibilities, Proc American Society of Civil Engineers, ASCE, New York, 1972.
[9] T.H. Almusallam, H.M. Elsanadedy, H. Abbas, S.H. Alsayed, Y.A. Al-Salloum, Progressive collapse analysis of a RC building subjected to blast loads, Struct. Eng. Mech. 36 (3) (2010) 301–319.
[10] H.M. Elsanadedy, T.H. Almusallam, Y.R. Alharbi, Y.A. Al-Salloum, H. Abbas, Progressive collapse potential of a typical steel building due to blast attacks, J. Constr. Steel Res. 101 (2014) 143–157.
[11] S.M. Baldridge, F.K. Humay, Reinforced concrete and secure buildings: progressive collapse, in: The Structural Bulletin Series, Concrete Reinforcing Steel Institute, 2004. No. 2.
[12] J. Choi, D. Chang, Prevention of progressive collapse for building structures to member disappearance by accidental actions, J. Loss Prevent. Proc. 22 (2009) 1016–1019.
[13] Y.A. Al-Salloum, T.H. Almusallam, M.Y. Khawaji, T. Ngo, H.M. Elsanadedy, H. Abbas, Progressive collapse analysis of RC buildings against internal blast, Adv. Struct. Eng. 18 (12) (2015) 2181–2192.
[14] P.X. Dat, T.K. Haiand, Y. Jun, A simplified approach to assess progressive collapse resistance of reinforced concrete framed structures, Eng. Struct. 101 (2015) 45–57.
[15] Y. Bao, S.K. Kunnath, S. El-Tawil, H.S. Lew, Macromodel-based simulation of progressive collapse: RC frame structures, J. Struct. Eng., ASCE 134 (7) (2008) 1079–1091.
[16] M. Sasani, M. Bazan, S. Sagiroglu, Experimental and analytical progressive collapse evaluation of actual reinforced concrete structure, ACI Struct. J. 104 (6) (2007) 731–739.
[17] J. Yu, K. Tan, Experimental and numerical investigation on progressive collapse resistance of reinforced concrete beam column sub-assemblages, Eng. Struct. 55 (2013) 90–106.
[18] M. Li, M. Sasani, Integrity and progressive collapse resistance of RC structures with ordinary and special moment frames, Eng. Struct. 95 (2015) 71–79.
[19] T. Wang, Q. Chen, H. Zhao, L. Zhang, Experimental study on progressive collapse performance of frame with specially shaped columns subjected to middle column removal, Shock Vib. (2016) 13 7956189.
[20] S.B. Kang, K.H. Tan, Behaviour of precast concrete beam-column sub-assemblages subject to column removal, Eng. Struct. 93 (2015) 85–96.
[21] S.B. Kang, K.H. Tan, E. Yang, Progressive collapse resistance of precast beam-column sub-assemblages with engineered cementitious composites, Eng. Struct. 98 (2015) 186–200.
[22] R.B. Nimse, D.D. Joshi, P.V. Patel, Behavior of wet precast beam column connections under progressive collapse scenario: an experimental study, Int. J. Adv. Struct. Eng. 6 (2014) 149–159.
[23] L.F. Maya, C. Zanuy, L. Albajar, C. Lopez, J. Portabella, Experimental assessment of connections for precast concrete frames using ultra high performance fibre reinforced concrete, Constr. Build. Mater. 48 (2013) 173–186.
[24] G. Magliulo, M. Ercolino, M. Cimmino, V. Capozzi, G. Manfredi, FEM analysis of the strength of RC beam-to-column dowel connections under monotonic actions, Constr. Build. Mater. 69 (2014) 271–284.
[25] American Society of Civil Engineers (ASCE), Blast protection of buildings, ASCE/SEI 59-11, 2011.
[26] DoD, Design of building to resist progressive collapse, United facilities criteria (UFC), UFC 4-023-03, Department of Defense, USA, 2013.
[27] IBC. International building code 2015, International Code Council, Inc., International conference of building officials, Whittier, CA, 2015.
[28] GSA, Alternate path analysis & design guidelines for progressive collapse resistance, General Services Administration, USA, 2013.
[29] NBCC. National building code of Canada 2015, National Research Council of Canada, Ottawa, Canada, 2015.
[30] Livermore Software Technology Corporation (LSTC), LS-DYNA user's keyword manual (nonlinear dynamic analysis of structures in three dimensions) Volume 1. Version 971, LSTC, Livermore, CA, 2007.

[31] ASTM, Standard test method for compressive strength of cylindrical concrete specimens. ASTM C39/C39M, American Society for Testing and Materials, West Conshohocken, PA, USA, 2010.

[32] ASTM, Standard test methods for tension testing of metallic materials. ASTM E8/E8M, American Society for Testing and Materials, West Conshohocken, PA, USA, 2009.

[33] T.B. Belytschko, C.S. Tsay, Explicit algorithms for non-linear dynamics of shells, J. Appl. Mech., ASME 48 (1981) 209–231.

[34] Y.D. Murray, A. Abu-Odeh, R. Bligh, Evaluation of concrete material model 159 Report No. FHWA-HRT-05-063, US Department of Transportation, Federal Highway Administration National Transportation Systems Center, USA, 2007.

[35] R.M. Christensen, A nonlinear theory of viscoelasticity for application to elastomers, J. Appl. Mech., ASME 47 (1980) 762–768.

[36] H.M. Elsanadedy, T.H. Almusallam, S.H. Alsayed, Y.A. Al-Salloum, Flexural strengthening of RC beams using textile reinforced mortar – experimental and numerical study, Compos. Struct. 97 (2013) 40–55.

[37] ACI Committee 318, Building code requirements for structural concrete and commentary. ACI 318-14, American Concrete Institute, Detroit, MI, USA, 2014.

[38] California Department of Transportation (Caltrans), Memo to designers 7-1 (Bridge Bearings), June 1994, p. 69.

[39] J. Silfwerbrand, Shear bond strength in repaired concrete structures, Mater. Struct. 36 (2003) 419–424.